SECONDARY INSTABILITIES IN A LAMINAR SEPARATION BUBBLE

U. Maucher, U. Rist, S. Wagner
Universität Stuttgart, Institut für Aerodynamik und Gasdynamik
Pfaffenwaldring 21, D-70550 Stuttgart, Germany

SUMMARY

If a strong adverse pressure gradient is imposed on an initially laminar boundary layer, it is decelerated and eventually separates. In this case, disturbances are strongly amplified and finally transition to turbulence takes place. Thus, a strong exchange of high-momentum fluid far away from the wall and low-momentum fluid near the wall is forced and re-attachment may occur. Besides this more general understanding of the physics of laminar separation bubbles (LSB), detailed knowledge of the transition to turbulence in a LSB is still missing. In Direct Numerical Simulations (DNS) artificial 2-D and 3-D disturbances are excited. If the size of the bubble is sufficiently large, DNS with realistic 2-D amplitude but very low initial 3-D amplitude indicate temporal amplification of the 3-D disturbances. Depending on the spanwise wavenumber, the self excited 3-D disturbances are either subharmonic or fundamental with respect to the 2-D disturbance. Subsequently, the spatio-temporal development of the 3-D disturbances is analyzed in order to find the source of their amplification.

NUMERICAL METHOD

The numerical method was developed in the research-group "Transition and Turbulence" of the Institut für Aerodynamik und Gasdynamik IAG [5],[3]. It is based on the complete, incompressible Navier-Stokes equations in vorticity-velocity formulation. A flat-plate boundary-layer is subjected to an adverse pressure gradient by prescribing the potential velocity u_p at the upper boundary of a rectangular integration domain (figure 1). At the inflow boundary there is stationary flow. In a disturbance strip at the wall, artificial 2-D and 3-D disturbances can be excited by periodic, wall-normal suction and blowing. At the outflow boundary boundary-layer assumptions are made. Upstream of the outflow boundary a buffer domain is applied, which damps the unsteady component of the flow smoothly to zero [4]. Thus, reflections at the outflow boundary can be suppressed.
All dimensional variables (marked by bars) are non-dimensionalized in the usual manner by a length length scale $\overline{L}$, the velocity $\overline{U}_\infty$, and the Reynolds number $Re = \frac{\overline{U}_\infty \overline{L}}{\overline{\nu}}$.
The time-integration of the non-dimensionalized Navier-Stokes equations in vorticity-transport formulation

$$\frac{\partial \omega_x}{\partial t} + \frac{\partial}{\partial y}(v\omega_x - u\omega_y) + \frac{\partial}{\partial z}(w\omega_x - u\omega_z) = \frac{1}{Re}\frac{\partial^2 \omega_x}{\partial x^2} + \frac{\partial^2 \omega_x}{\partial y^2} + \frac{1}{Re}\frac{\partial^2 \omega_x}{\partial z^2} \tag{1}$$

$$\frac{\partial \omega_y}{\partial t} - \frac{\partial}{\partial x}(v\omega_x - u\omega_y) + \frac{\partial}{\partial z}(w\omega_y - v\omega_z) = \frac{1}{Re}\frac{\partial^2 \omega_y}{\partial x^2} + \frac{\partial^2 \omega_y}{\partial y^2} + \frac{1}{Re}\frac{\partial^2 \omega_y}{\partial z^2} \tag{2}$$

$$\frac{\partial \omega_z}{\partial t} + \frac{\partial}{\partial x}(u\omega_z - w\omega_x) + \frac{\partial}{\partial y}(v\omega_z - w\omega_y) = \frac{1}{Re}\frac{\partial^2 \omega_z}{\partial x^2} + \frac{\partial^2 \omega_z}{\partial y^2} + \frac{1}{Re}\frac{\partial^2 \omega_z}{\partial z^2} \tag{3}$$

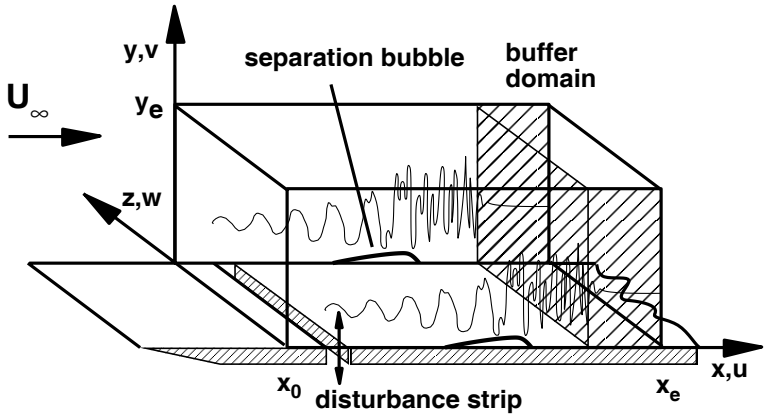

Wall-normal direction scaled with $\sqrt{Re}$.
Non-dimensionalized vorticity:

$$\begin{aligned} \omega_x &= \frac{1}{Re}\frac{\partial v}{\partial z} - \frac{\partial w}{\partial y} \\ \omega_y &= \frac{\partial w}{\partial x} - \frac{\partial u}{\partial z} \\ \omega_z &= \frac{\partial u}{\partial y} - \frac{1}{Re}\frac{\partial v}{\partial x} \end{aligned}$$

Fig. 1 Integration Domain

is performed with a fourth-order accurate Runge-Kutta scheme. The four stages per time step are coupled with an alternating upwind-downwind (and vice versa) discretisation of the x-convection terms. Thus, the scheme is of 4th-order accuracy in time and space and insufficiently resolved oscillations (wiggles) are numerically damped.
In spanwise direction a spectral approach which exploits periodicity is used:

$$f(x,y,z,t) = \sum_{k=-K}^{K} F_k(x,y,t)e^{ik\gamma z}, \tag{4}$$

where γ is the basic spanwise wavenumber defined by $\gamma = 2\pi/\lambda_z$. In experiments this assumption has been shown to be in good agreement with physics of boundary layer flows [2]. Assuming spanwise symmetry of the 3-D disturbance development, only the spectral modes from $k = 0$ (2-D) to $k = K$ have to be regarded.
The velocity components can be obtained by solving three Poisson-equations:

$$\frac{\partial^2 u}{\partial x^2} + \frac{\partial^2 u}{\partial z^2} = -\frac{\partial \omega_y}{\partial z} - \frac{\partial^2 v}{\partial x \partial y}, \tag{5}$$

$$\frac{\partial^2 w}{\partial x^2} + \frac{\partial^2 w}{\partial z^2} = \frac{\partial \omega_y}{\partial z} - \frac{\partial^2 v}{\partial y \partial z}, \tag{6}$$

$$\frac{1}{Re}\frac{\partial^2 v}{\partial x^2} + \frac{\partial^2 v}{\partial y^2} + \frac{1}{Re}\frac{\partial^2 v}{\partial z^2} = \frac{\partial \omega_x}{\partial z} - \frac{\partial \omega_z}{\partial x}. \tag{7}$$

Central finite differences with 4th order accuracy are applied for the x- and y-derivatives. A penta-diagonal system coupled only in x is solved for each line $y = const.$ to obtain u (equation 5) and w (equation 6). A line Gauss-Seidel scheme accelerated by multigrid is applied to effectively solve the v-Poisson equation. Nevertheless, the iteration of the v-velocity requires 60% of the total CPU-time.
The 2-D component of the downstream velocity u is integrated from the continuity equation:

$$u_{k=0}(x,y) = u_{k=0}(x_0,y) - \int_{\xi=x_0}^{x} \frac{\partial v_{k=0}}{\partial y} d\xi. \tag{8}$$

The numerical code is well adapted to the computer architecture used for the calculations (NEC SX-4: 32 CPUs, vector architecture, shared memory, peak-performance/CPU = 2

GigaFLOPS). In serial mode the performance of the code is approximately 1150 MFLOPS, i.e. 58 % of the peak performance. Optionally, the nonlinear terms are calculated in parallel on lines with $y = const.$ Apart from these terms, the k-harmonics of the spectral ansatz are independent from each other and can be treated in parallel. In parallel computations, the performance per CPU decreases only slightly to $\approx$ 1100 MFLOPS/CPU. Calculating with K=10 (11 CPUs) a speedup of about 10 is achieved. This is important for the parametric studies performed further down.

DIRECT NUMERICAL SIMULATION (DNS), 2-D BASE FLOW

The DNS is performed in two steps. In a first step, a "base flow" with separation bubble is calculated in a 2-D simulation. Spatially amplified Tollmien-Schlichting waves (frequency ($\beta_0 = 10$) are excited by periodic suction and blowing at the wall. In the second step, the development of 3-D disturbances in this two-dimensional, periodic flow is examined. The 2-D "base flow" is addressed in this section, the 3-D disturbance development in the following sections.

In experiments in the Laminar Wind Tunnel of the IAG [7], a LSB on a wing section with a chord-length of $\overline{c} = 0.615\ m$ was investigated. The chord Reynolds number was $Re_c = 1.2 * 10^6$. The 2-D DNS aims at calculating a LSB with comparable physical properties. The free-stream velocity $\overline{U}_\infty$ is $29.3\frac{m}{s}$. In DNS the reference length $\overline{L}$ is chosen to be $6.15\ cm$. Hence, the Reynolds number is 120000, the chord length $c = \overline{c}/\overline{L} = 10$. In 2-D DNS the generation of turbulence and the related fine-scale eddies is suppressed by the absence of three-dimensionality. However, saturated large-scale vortices effect the momentum transport towards the wall, which is necessary to force re-attachment. The size of the bubble is influenced by the initial disturbance amplitude. The lower it is, the later disturbances gain nonlinear amplitude and subsequently the separation bubble grows in length and reverse-flow intensity.

In the experiments, two velocity distributions $u_e(x)$ at the edge of the boundary layer have been measured (figure 2a). The first one (squares) refers to a flow with separation bubble. For the second, turbulent one, separation has been suppressed by fixing a turbulator upstream of the separation bubble (triangles). In DNS, the upper boundary of the integration domain is far away from the boundary layer and is situated in the potential flow. In former simulations, it turned out that due to displacement effects caused by the separation bubble, the velocity distribution at the edge of the boundary layer yields a

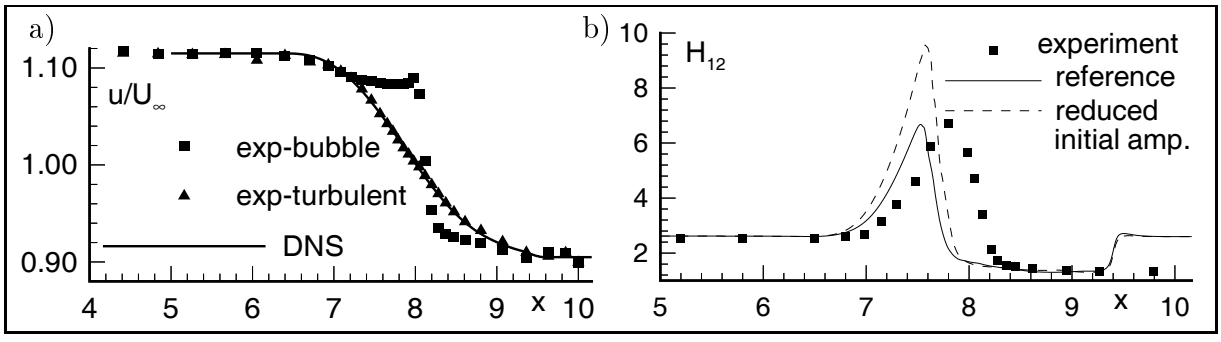

Fig. 2 Comparison of a) the edge-velocity distribution and b) the shape parameter in the experiment (symbols) and the DNS.

typical "separated" pressure plateau at the location of the bubble, and differs from the upper boundary condition u_p. For that reason, the turbulent distribution was chosen as upper boundary condition for the DNS (solid line).
In the present calculations however, a very fine grid is necessary to accurately resolve the flow. Therefore the height of the integration domain was restricted by memory and CPU-time requirements. Thus, the upper boundary is rather close to the boundary layer and has strong impact on re-attachment. Consequently, the edge velocity in the simulation is only slightly varied by displacement effects but strongly influenced by the upper boundary. The major interest of the calculations presented here, is to examine stability properties of the spatio-temporal disturbance development. Differences between the experimental and numerical mean-flow have been accepted. In figure 2b, the shape parameter H_{12} for DNS with two different initial disturbance amplitudes is compared to the experimental data (symbols). The computed separation occurs upstream of the location in the experiment and the bubble is shorter, due to the aforementioned suppression of displacement effects. The length of the bubble changes only moderately if the initial disturbance amplitude is decreased (from $u' \approx 10^{-4}$ (solid line) to $\approx 10^{-5}$ (dashed), for example). In contrast, with lower disturbance-amplitude the maximum of H_{12} dramatically increases. The H_{12}-maximum of the solid curve is quite close to the experimental maximum. Therefore, this case is regarded to be in better agreement with the experiment and is chosen for the 3-D DNS.

DIRECT NUMERICAL SIMULATION, 3-D DISTURBANCES

The periodic "base flow" is superposed by 3-D disturbances with very small amplitude ($u' \approx 10^{-10}$). Amplification curves (figure 3a) show the spatial development of the 2-D wave (solid line) and the 3-D wave (dashed). The respective higher harmonics are depicted by the dotted lines. Both waves are excited in the disturbance strip. Subsequently they propagate downstream and are convectively amplified by linear instability. As the 2-D wave gains a nonlinear amplitude ($\approx 1\%$ of U_∞) strong nonlinear amplification (secondary

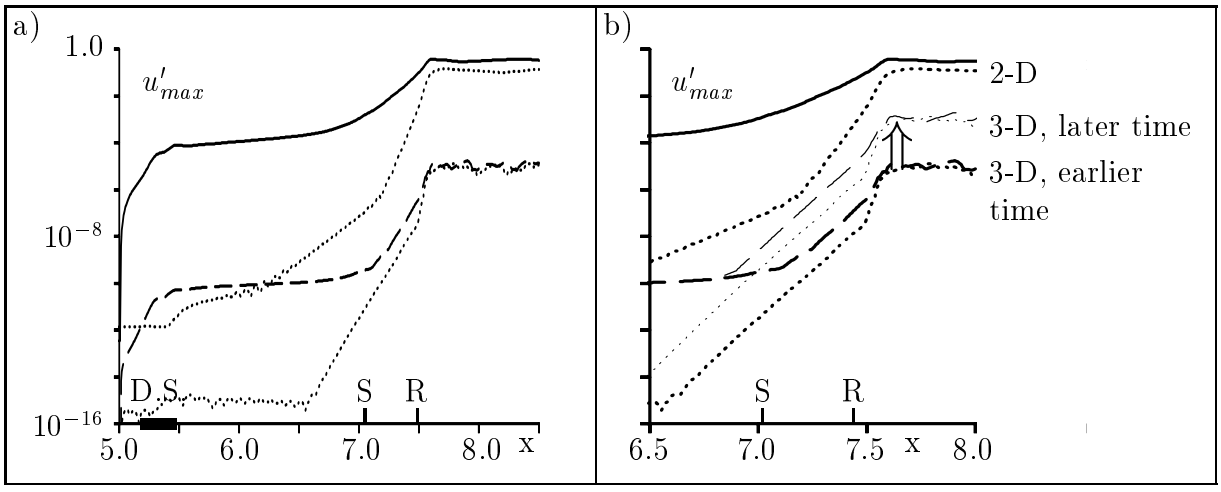

Fig. 3 a) Disturbance amplitude of 2-D (solid) and 3-D (dashed) waves b) vicinity of the bubble. Dotted lines: higher harmonics. Arrow: 3-D temporal growth. S - separation, R - re-attachment. D.S.: disturbance strip.

instability, see Herbert [1]) of the 3-D wave sets in. Finally, the 2-D wave saturates in the re-attachment zone (separation and re-attachment indicated by S and R) and the nonlinear amplification of the 3-D modes vanishes, as well.
A close-up view of the disturbance amplitudes in the vicinity of the separation bubble is plotted in figure 3b. Additional thin lines show the amplitude of the 3-D modes at a later disturbance cycle. For $x < 6.8$, the amplitudes do not differ in both periods shown in the plot. The disturbances propagate downstream in a convective manner. In the separation bubble, however, the amplitude curves exhibit temporal growth of the 3-D modes (arrow). This is in contrast to separation bubbles at lower Reynolds numbers [6]. Indeed, the temporal growth rate is very low compared to the spatial growth rate α_i which is in this domain about 20 – 40 times the temporal rate β_i.
Interestingly, the nonlinear interaction of the 2-D wave with frequency $\beta_0 = 10$ and a wave-number of $\alpha \approx 20$ and 3-D modes with different spanwise wave-numbers γ yields two different temporally amplified 3-D waves, as can be seen in figure 4:

1. "Subharmonic" disturbances (dash-dotted line):
   a 3-D mode with the frequency $\beta = 1/2 * \beta_0$ and the respective higher harmonics $(\frac{2n+1}{2} * \beta_0)$ are generated; the spanwise wave number is: $\gamma_{sub} \approx \alpha$.

2. "Fundamental" disturbances (solid line):
   a longitudinal vortex and a 3-D mode with the frequency $\beta = \beta_0$ (and the higher harmonics $n * \beta_0$); the spanwise wave number is: $\gamma_{fun} > \gamma_{sub}$.

The quotes are used to distinguish the underlying mechanisms from the amplification due to fundamental and subharmonic secondary instability in the sense of Herbert [1] which would yield the same kind of 3-D disturbances but without temporal amplification. The calculation for $\gamma = 16$ showed no temporal amplification. Therefore, the dash-dotted line in fact consists of only one point ($\gamma = 20$ and the information that $\beta_{i,\gamma=16} < 0$).
The numerical scheme has been extensively tested. In order to obtain figure 4, 3-D disturbances were excited for only a short period of time in the separation bubble i.e., it is sufficient to force the 3-D disturbances only once to obtain the disturbances mentioned above. In any case, the 2-D wave is continuously excited.
Elimination of possible reflections at the inflow boundary in an additional damping zone between that boundary and the disturbance strip did not affect β_i. To exclude influences

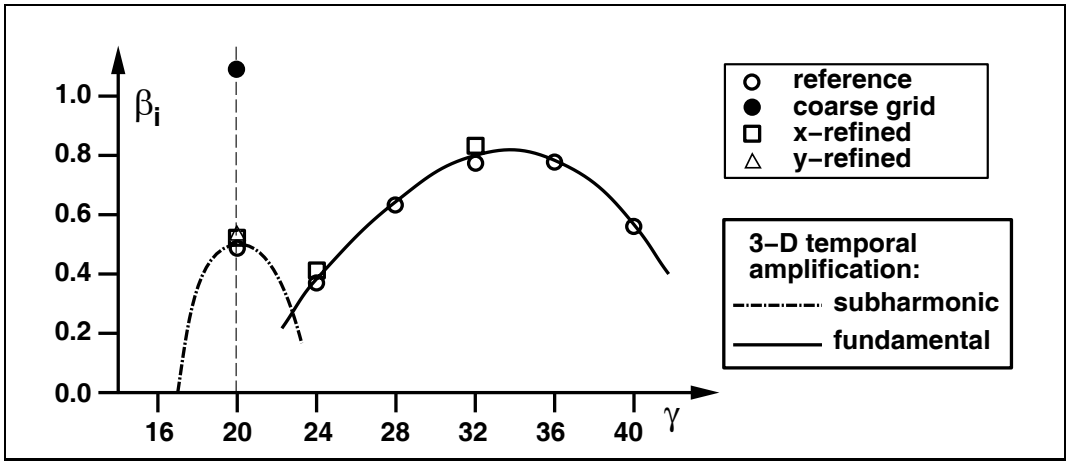

Fig. 4 Dependency of temporal amplification from the spanwise wavenumber γ. Grid-refinement study at $\gamma = 20$ (dashed line).

of the outflow boundary condition a test calculation with a very long integration domain has been performed. The 3-D disturbances in the bubble exhibit the in the shorter domain observed growth rate β_i, before the first disturbances reach the outflow boundary. Finally, the influence of the spatial discretisation was investigated for a fixed spanwise wavenumber $\gamma = 20$. The grid was refined from coarse to the reference and an even finer x-spacing by a factor of two, respectively. Additionally, the reference discretisation was refined in the wall-normal direction by a factor of two. With the coarse grid (figure 4, filled circle), the amplification rate β_i strongly differed from the other cases. In contrast, the refinement of the reference grid showed only negligible influence on the growth rate β_i (triangle and square on the dashed line). Comparisons of the amplification rate β_i for $\gamma = 24$ and $\gamma = 32$ calculated with the reference grid (circles) and the x-refined grid (squares) confirm this observation. Thus, results with the reference discretisation can be regarded as grid-independent.

To further investigate the origin and the properties of the temporal 3-D growth, the 3-D component of the velocity u is analyzed. Since the amplitude changes spatially and temporally, it is necessary to normalize u to compare the time signals at different streamwise locations. The velocity in the whole y,t-domain for a specific x-location is normalized with the maximum value in this plane. If the resulting velocity u_{norm} is plotted in a x,t-diagram, the spatio-temporal development can be investigated. Figure 5a shows this representation of u_{norm} in the "subharmonic" case ($\gamma = 20$) at a constant distance from the wall ($y = 0.93$) and on the centerline ($z = 0$). Due to the spanwise spectral ansatz, at $z = \pm\lambda_z/2$ the velocity is exactly the same with opposite sign. The spatial x-axis is horizontal, the time axis is vertical. Consequently, streaks from lower left to top right (positive gradient) denote convective (downstream) disturbance motion, and streaks with negative gradient indicate upstream influence. The time signals of four characteristic streamwise positions, marked by bold lines, are plotted in figure 5b.

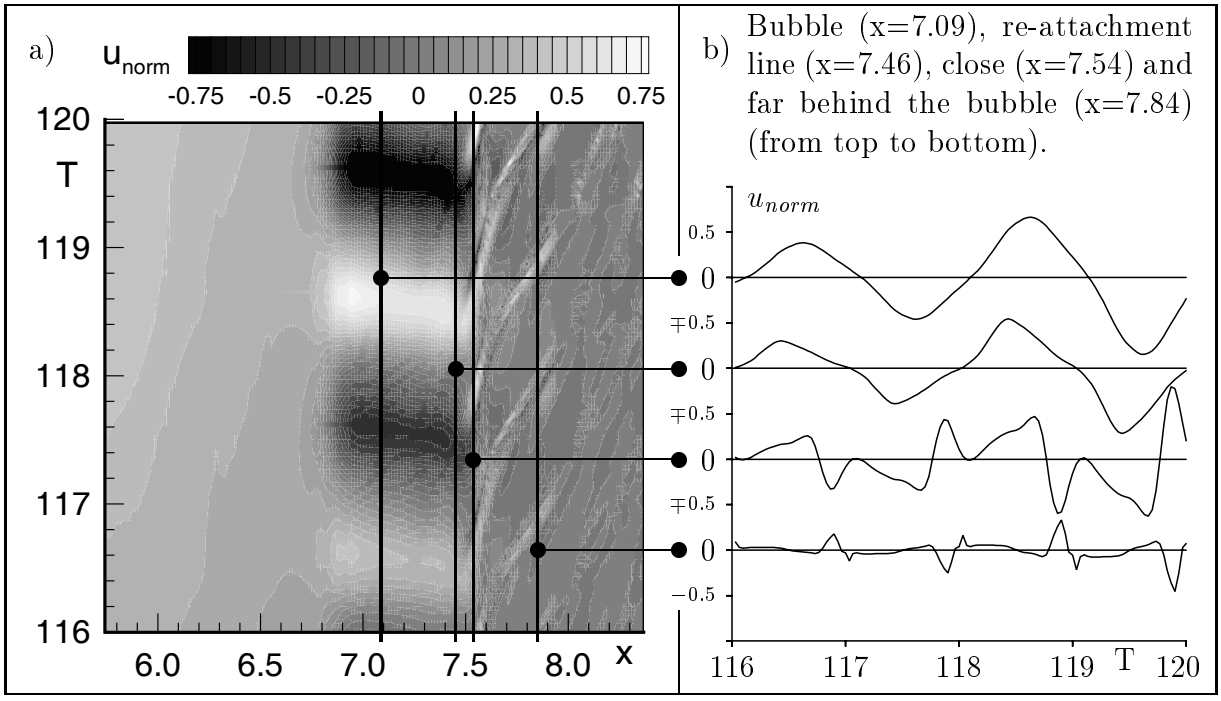

Fig. 5 'Subharmonic' growth ($\gamma = 20$, $y = 0.93$, T: period of the 2-D waves): a) temporal-spatial development of the 3-D velocity in constant wall-distance, b) time-signals.

In the bubble ($7.04 < x < 7.46$) the x,t-gradient is negative. Disturbances propagate upstream with high velocity. The stronger contrast in the upper part of the plot highlights the temporally increasing amplitude. For $x > 7.5$, streaks with positive gradient are apparent. In this region, the flow is dominated by convection. The time signals significantly change when the re-attachment line ($x = 7.46$) is passed. In the bubble and at the re-attachment line, the subharmonic frequency dominates (two top curves). The nonlinear interaction between 2-D and 3-D modes and correspondingly the generation of higher harmonics is weak. Behind the bubble, however, the amplitude of the higher harmonics is very large due to the saturated 2-D wave (figure 3).
The phase and amplitude of the disturbance profiles of the "subharmonic" case ($\gamma = 20$) and the "fundamental" case ($\gamma = 32$) are plotted in figure 6. Since the time signal is normalized to one, the contribution of the Fourier harmonics to the total time signal can be easily recognized. In the "subharmonic" case (solid lines) the bubble is dominated by the subharmonic oscillation. Vortex structures (weak phase shift), with a rotation centerline almost parallel to the x-axis, expand with large velocity from the re-attachment zone into the bubble and change their sign periodically. Downstream of the bubble, the subharmonic oscillation looses influence. Finally, at $x = 7.84$ its amplitude is less than 0.2 related to the local disturbance amplitude. In contrast to the "subharmonic" case, the longitudinal vortices (dotted line) have large impact on the "fundamental" mechanism. In the bubble, their amplitude is approximately three times the amplitude of the fundamental oscillations (dash-dotted). Pairs of counter-rotating longitudinal vortices dominate the bubble.
Typical eigenfunctions (profiles) of classical linear stability theory and of secondary stability theory are characterized by changes of the sign of the amplitude and a corresponding phase shift of π. While the disturbance profiles in the "subharmonic" do not indicate any such profiles, they are present in the "fundamental" case in the close vicinity of the re-attachment line ($x = 7.46,\ x = 7.54$). Nevertheless, this region is so small, that it seems very unlikely that amplification according to classical linear or secondary instability theory is involved in the observed phenomena. At $x = 7.84$, the profiles of the "fundamental" mechanism are quite similar to the "subharmonic" profiles. In any case, the 3-D behavior is dominated by the 2-D periodic "base flow".
The observed 3-D temporal amplification very likely originates from a new type of sec-

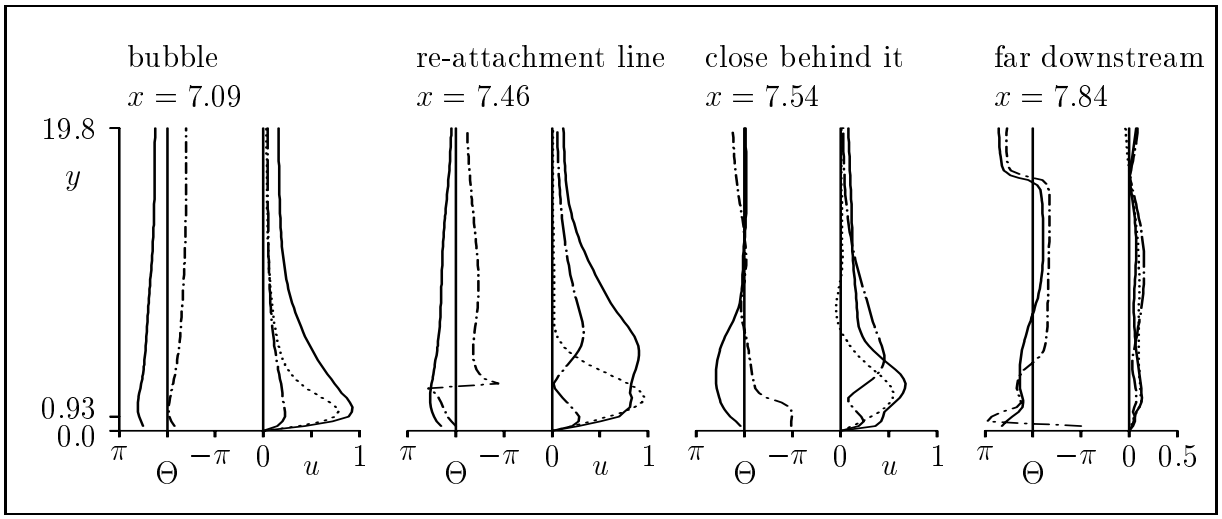

Fig. 6 Comparison of 3-D profiles of the "subharmonic" (solid lines) and the "fundamental" (wave: dash-dotted and longitudinal vortex: dotted) 3-D disturbances.

ondary instability which leads to a spanwise deformation of the large-amplitude TS-wave or "vortices" in the re-attachment region. Thus, the re-attachment line is oscillating in the "subharmonic" case, whereas the increasing deformation due to the longitudinal vortices is only modulated by the fundamental wave in the "fundamental" case.

CONCLUSION

DNS of a laminar separation bubble exhibit temporal amplification of 3-D modes by interaction with a nonlinear 2-D wave. Compared to the 2-D frequency, this growth can be subharmonic or fundamental. Disturbance waves are only observed in the "fundamental" case, and only in a very localized region near the re-attachment line. There are no hints on amplification due to classical linear stability theory or secondary stability theory. The re-attachment region is the origin of disturbances propagating upstream as well as of waves convecting downstream. Referring to the present knowledge, the re-attachment region therefore has to be considered as the source of the temporal growth of the 3-D modes. To obtain better insight into the wake of laminar separation bubbles, the simulations of both mechanisms will be continued until the temporal amplification leads to transition. Longitudinal vortices behind the bubble for instance, which have been observed in many experiments, might be due to the "fundamental" mechanism observed here.

ACKNOWLEDGEMENTS

This research is supported by the Deutsche Forschungsgemeinschaft DFG under contract number Ri 680/1-1,2.

REFERENCES

[1] HERBERT, T.: "Secondary instability of boundary layers", Ann. Rev. of Fluid Mech., 20 (1988), pp. 487–526. 1988.

[2] KACHANOV, Y. S.: "Physical mechanisms of laminar-boundary-layer transition" Ann. Rev. Fluid Mech., 26 (1994), pp. 359–391.

[3] KLOKER, M.: "Direkte Numerische Simulation des laminar-turbulenten Strömungsumschlages in einer stark verzögerten Grenzschicht", Dissertation, Universität Stuttgart, 1993.

[4] KLOKER, M., KONZELMANN, U., FASEL, H.: "Outflow boundary conditions for spatial Navier-Stokes simulations of transition boundary layers", AIAA J., 31(4) (1993), pp. 620–628.

[5] RIST, U., FASEL, H.: "Direct numerical simulation of controlled transition in a flat-plate boundary layer", J. Fluid Mech., 298 (1995), pp. 211–248.

[6] RIST, U., MAUCHER, U., WAGNER, S.: "Direct Numerical Simulation of Some Fundamental Problems Related to Transition in Laminar Separation Bubbles", Computational Fluid Dynamics '96, John Wiley & Sons Ltd., 1996, pp. 319–325.

[7] WÜRZ, W., WAGNER, S.: "Experimental Investigations of Transition-Development in attached Boundary-Layers and Laminar Separation Bubbles", NNFM, this volume.